

Solid-state plastic deformation in the dynamic interior of a differentiated asteroid

B. J. Tkalcec^{1*}, G. J. Golabek^{2,3}, F. E. Brenker¹

¹Geoscience Institute, Goethe University, Altenhöferallee 1, 60438 Frankfurt am Main, Germany. *tkalcec@em.uni-frankfurt.de

²ENS Lyon, Laboratoire de Géologie, 46 Allée d'Italie, 69364 Lyon Cedex 07, France.

³ETH Zürich, Institute of Geophysics, Sonneggstrasse 5, 8092 Zürich, Switzerland.

This supplementary online information includes:

Section S1: Supplementary EBSD data and analytical methods.

Supplementary Fig. S1: EBSD data of NWA 5480 Zones A and B

Supplementary Table S1: Fabric description

Section S2: Supplementary data: Solidification of the HED parent body

Supplementary Fig. S2: Thermal evolution at different depths

Section S3: Supplementary description of the numerical methods

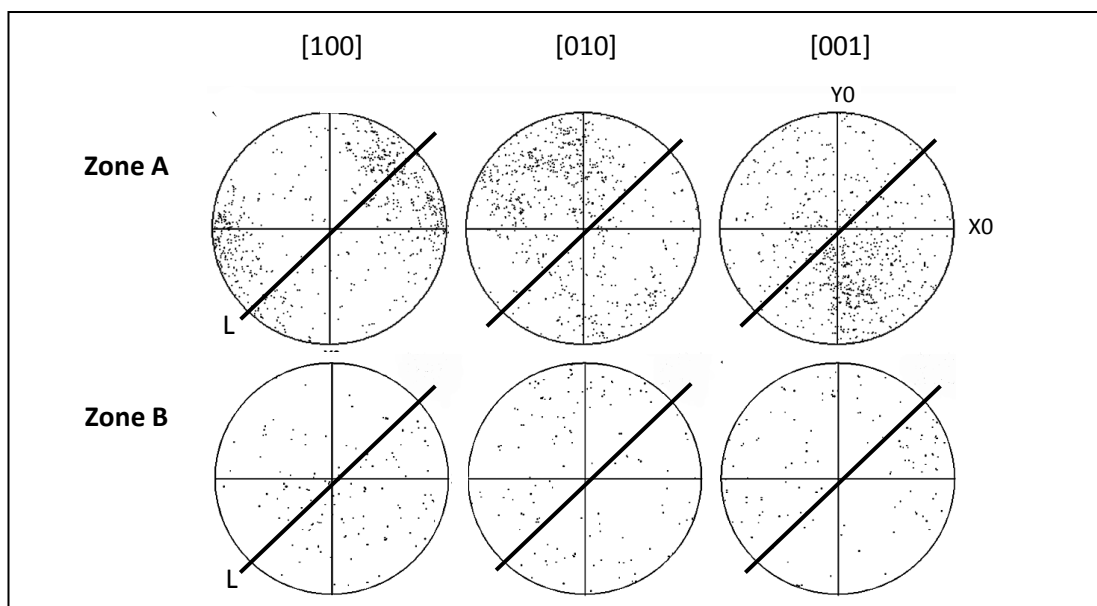
Supplementary Table S2: Model Overview

Supplementary Table S3: Physical Parameters

Section S4: Supplementary references

S1. Supplementary EBSD Data and Analytical Methods

The EBSD results of olivine crystals measured in Zones A and B of NWA 5480 are presented here (Supplementary Fig. S1) in scattered data form showing each individual measurement.




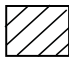

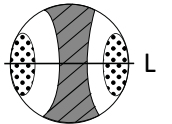
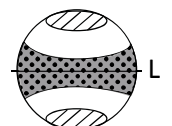
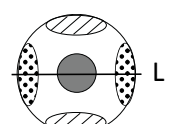
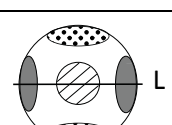
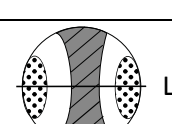
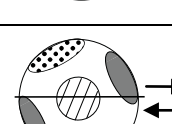
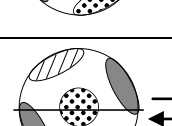
Supplementary Fig. S1: EBSD results of olivine crystals in Zones A and B of NWA 5480: Raw EBSD data of NWA 5480 analysis are displayed as scattered data plots in upper hemisphere, equal area, stereographic projections. The results are displayed according to the orientation of the main olivine crystallographic axes [100], [010] and [001]. The olivine-dominated Zone A shows a total of 1361 diffraction measurements of the (coarse-grained) olivine. The schlieren-dominated Zone B shows a total of 148 diffraction measurements of the (finer-grained) olivine. Solid black line denotes the presumed NE-SW foliation. L denotes the lineation. The coordinate system (X0, Y0) relates to the edges of the sample.

The stage was moved manually to 58 different sample locations in Zone A (and 20 locations in Zone B). The working distance was 20 mm. In Zone A about 15-25 olivine diffraction patterns were recorded over the area of each sample location. In Zone B about 5-10 olivine diffraction patterns were recorded over the area of each sample location. The diffraction pattern yielded by each measurement was assessed individually for accuracy of indexing before being discarded or saved. Indexing was based upon a minimum of 5 and a maximum of 7 bands. Only indexing with a mean angular deviation (MAD) <1.0 was accepted and recorded. The EBSD measurements were performed manually without the use of automated mapping options.

S1.1 Comparison of LPO measured for the olivine in NWA 5480 Zone A with those found in olivine in common terrestrial peridotites.

In Figure 3 of the main text, the measured axes orientations of NWA 5480 Zone A are compared with compilations of observed LPOs from common terrestrial mantle rocks. For ease of comparison, each LPO (consisting of axes-plots of the three main olivine axes [100], [010] and [001]) has been summarized into a schematic diagram and rotated to show the foliation as horizontal. The fabrics of the LPOs are described in detail for comparison in Supplementary Table S1. The three axes-plots are depicted in each case as spotted [100], striped [010] and solid grey [001] respectively, the foliation is denoted by a solid black line and the lineation is denoted by L.

Supplementary Table S1: Fabric description of the olivine LPOs of NWA 5480 Zone A and other common terrestrial mantle rocks.

	Comment	[100] spotted 	[010] striped 	[001] solid grey 	LPO — Foliation L Lineation
(a)	NWA 5480 Zone A	Point maxima within the foliation, parallel to the lineation	Broad girdle normal to lineation	Broad girdle normal to lineation	
(b)	Oman Ophiolite ^{S1} (cumulate, compaction)	Girdle within the foliation	Point maxima normal to foliation	Girdle within the foliation	
(c)	Most common LPO (010)[100] ^{S2,S3}	Point maxima within the foliation, parallel to the lineation	Point maximum normal to foliation	Point maxima within the foliation, normal to the lineation	
(d)	Further common LPO (100)[001] ^{S4}	Point maxima normal to foliation	Point maxima within the foliation, normal to lineation	Point maxima within the foliation, parallel to lineation	
(e)	Pencil Glide {0kl}[100] ^{S2,S3}	Point maxima within the foliation, parallel to the lineation	Broad girdle normal to lineation	Broad girdle normal to lineation	
(f)	Experimental results of dextral shear under hydrous conditions ^{S5}	Point maxima strongly oblique to shear direction	Point maxima normal to the shear direction	Point maxima subparallel to shear direction	
(g)	Experimental results of dextral shear with 6 % melt ^{S6}	Point maxima normal to the shear direction	Point maxima strongly oblique to shear direction	Point maxima subparallel to shear direction	

^{S1}summarized and adapted from original data from Boudier, (1991)^{S1}

^{S2}summarized and adapted from original data of Ismail & Mainprice (1998)^{S2}

^{S3}summarized and adapted from original data of Tommasi et al. (2000)^{S3}

^{S4}summarized and adapted from original data of Frese (2003)^{S4}

^{S5}summarized and adapted from original data of Jung et al. (2006)^{S5}

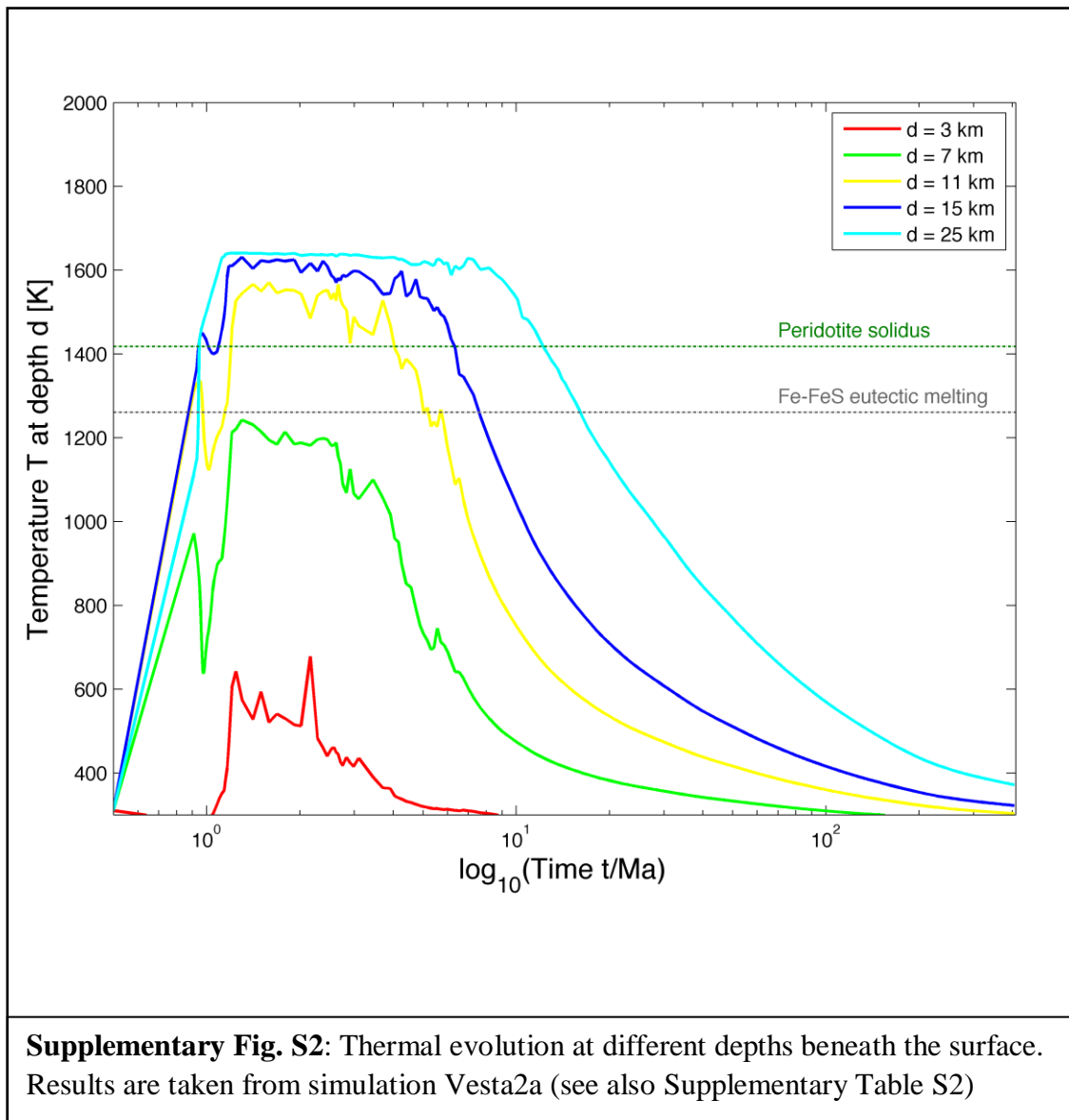
^{S6}summarized and adapted from original data of Holtzman et al. (2003)^{S6}

Supplementary Table S1(a) shows the resulting schematic LPO for the main crystallographic axes [100], [010] and [001] orientations in NWA 5480 Zone A. Our reference frame illustrates that for NWA 5480 the [100] axes plot parallel to the foliation, whereas the other two main crystallographic orientations [010] and [001] form broad girdles normal to the foliation. Supplementary Table S1(b)^{S1} summarizes an olivine LPO as measured in a wehrlite intrusion within the Oman ophiolite^{S1} showing a well-developed SPO fabric typical of compaction-style processes^{S1} with strong point maxima of [010] perpendicular to the foliation and [100] and [001] as girdles within the foliation. The LPO shown in Supplementary Table S1(c)^{S2,S3} shows the most common active glide system during terrestrial solid-state deformation, the (010)[100] slip system^{S2,S3}. It displays point maxima of [010] perpendicular to the foliation, but forms point maxima of [100] within the foliation parallel to the lineation and the third direction [001] shows point maxima within the foliation, normal to the lineation. The latter two axes do not coincide with the LPO measured for Zone A of NWA 5480 (S1(a)). A further common glide system (100)[001]^{S4} most active during solid-state plastic deformation forms the LPO shown in Supplementary Table S1(d)^{S4}. Here [100] axes form point maxima normal to the foliation, whereas [001] and [010] show point maxima within the foliation. The [001] axes plot parallel, the [010] axes normal to the lineation. Supplementary Table S1(e)^{S2,S3} summarizes the LPO generated by dunites and peridotites plastically deformed in the solid state by pencil glide whereby multiple {0kl}[100] glide systems are activated. It shows an LPO that matches the one measured in NWA 5480 Zone A (S1(a)). Supplementary Table S1(f)^{S5} summarizes the LPO generated by olivine aggregates experimentally deformed by dextral shear ($\gamma = 1.0$) under hydrous conditions (1300 ppm H/Si) at 1470 K and 1.9 GPa pressure. This type-C^{S5} fabric represents the (100)[001] slip system^{S5} and is similar to the (100)[001] in S1(d)^{S2,S3} yet with some backward rotation, opposite to the dextral shear direction. The [100] axes plot as point maxima strongly oblique to the direction of shear direction, the [010] axes plot as point maxima normal to the shear direction and the [001] axes plot as point maxima subparallel to the shear direction. Jung et al.^{S5} performed a range of experiments at 1470 K under varying water content and stress conditions and showed

that the addition of water first changes the fabric from type-A ((010)[100] slip system) to type-E ((001)[100] slip system) and then, at higher water content, type-C fabric ((100) [001] slip system). All the fabric types^{S5} resulting from deformation under hydrous conditions are distinctly different to the LPO measured in NWA 5480 Zone A (S1(a)) indicating the latter was deformed under anhydrous conditions with no influence of water. Finally, Supplementary Table S1(g)^{S6} summarizes the LPO generated by olivine experimentally deformed by dextral shear in the presence of 6% melt. The [100] axes plot as point maxima normal to the shear direction, the [010] axes plot as point maxima strongly oblique to the shear direction and the [001] axes plot as point maxima subparallel to the shear direction. This LPO is again very distinct from that in NWA 5480 Zone A (S1(a)) and reveals that the latter was not influenced by the presence of melt.

S.2 Solidification of the HED parent body

The timing of the solidification of the HED parent body is not well constrained and remains a topic of wide discussion with results ranging from <4 Ma^{S7,S8} to 100 Ma^{S9} after CAI formation. Although the subject of the thermal evolution of the HED parent body needs further investigation, the implications of the axes orientations measured for Zone A of NWA 5480 remain legitimate for almost any age within both end members of these proposed timescales. This is demonstrated by Supplementary Figure S2, which extracts from our numerical model the thermal evolution at different depths inside a Vesta-sized body. The grey and green lines mark the melting of eutectic Fe-FeS and peridotite, respectively. It clearly shows that at depths up to about 15 km, cooling below the peridotite solidus occurs within less than 10 Ma after CAI formation. This would be well within the maximum depth (about 50 km) at which the diogenite samples could be excavated by an impactor creating an impact basin comparable to the Rheasilvia basin at the Vestan south pole^{S10}.



S3 Supplementary Methods: Description of Numerical Modeling

We employ the 2D finite-difference numerical code I2MART^{S11} using a fully staggered grid and the marker-in-cell method. The computation domain is 1000 x 1000 km (grid resolution of 501 x 501 points with 4 million randomly distributed Lagrangian markers). The equations of gravity, momentum, mass and heat conservation are solved on the non-deforming Eulerian grid whereas the advection of transport properties including viscosity, temperature and melt fractions is performed on the moving Lagrangian markers.

The model assumes that the Vesta-sized planetesimal of 265 km radius^{S12} formed nearly instantaneously as suggested by the gravitational instability scenario^{S13}. In the numerical model the planetesimal is surrounded by a sticky air layer^{S14-S17} of nearly zero density, constant viscosity and constant temperature ($T_{sa} = 270 \text{ K}^{\text{S9}}$). This layer represents an infinite reservoir to absorb heat released from the planetary body^{S16} and ensures a free surface of the planetesimal^{S14-S17}. The formation date of the planetesimal is varied between 0 and 2 Ma after CAI formation, which is within geochemical restrictions for Vesta^{S18,S19}.

A temperature-, pressure-, strain-rate and melt-fraction dependent rheology based on parameters for dry olivine is used for the solid silicate component^{S20}. The release of potential energy due to planetesimal accretion^{S21} is assumed to increase the initial internal temperature of the planetesimal homogeneously. To compute the temperature distribution after iron-silicate differentiation, we distribute iron diapirs at the model start randomly throughout the interior of the planetesimal^{S16}. These iron diapirs form within less than 4 Ma a distinct iron-rich core, in general agreement with geochemical constraints^{S18,S19}. The iron/silicate fraction in the model is based on models of Vesta's interior^{S9}. To check the influence of the initial iron diapir size on the model result, the diapir radii are additionally varied between 10 and 25 km (see also Supplementary Table S2). No discernible effect on the general long-term thermal evolution was observed.

Melting of an eutectic iron-sulphur composition^{S22} and of dry peridotite^{S23,S24} is considered using a batch-melting model^{S25}. The model takes into account consumption, respectively release of latent heat due to melting and freezing of silicates and the iron-sulphur eutectic. For all models, we consider time-dependent radioactive heating by both short- (²⁶Al, ⁶⁰Fe) and long-lived radiogenic isotopes (⁴⁰K, ²³²Th, ²³⁵U, ²³⁸U) in the quantities suggested for CI chondrites^{S26}. Radiogenic isotopes are assumed to have partitioned into their preferred phase.

At a narrow silicate melt fraction range ζ_{crit} , the silicate behaviour undergoes a transition from a solid-like material to a low viscosity crystal suspension^{S27}. In the current study, we apply a sharp transition at a value of $\zeta_{crit} = 0.4$ ^{S28}. The viscosity of partially molten silicates was estimated to be in the range $\eta_{part} = 10^{16} - 10^{18}$ Pa s^{S29}. In the current study, we test the influence of this parameter on our results (see Supplementary Table S2). The general behaviour of the model was not influenced by the variation of this particular parameter.

At silicate melt fractions above the rheological transition, the viscosity of a largely molten magma ocean is expected to be $\eta_{Si-liq} = 10^{-4} - 10^2$ Pa s^{S30-S32}. This is significantly lower than the viscosities which can be treated in geodynamical models. The low viscosity results in an extremely vigorous convection and efficient heat loss from the magma ocean. However this efficient heat loss can be taken into account in the numerical model by using the increased thermal conductivity method^{S16, S33-S35} for largely molten silicates.

For this reason, we compute for silicate melt fractions larger than ζ_{crit} the expected heat flux q from a magma ocean applying the soft turbulence model^{S28,S36,S37}.

$$q = 0.089 \frac{k(T - T_{surf})}{L} Ra^{1/3} \quad (1)$$

where Ra is the Rayleigh number given by:

$$Ra = \frac{\alpha g (T - T_{surf}) \rho^2 c_P L^3}{k \eta_{Si-liq}} \quad (2)$$

α is the thermal expansivity of molten silicates, g is the local gravitational acceleration, T is the potential temperature, T_{surf} is the surface temperature, ρ is the effective density of the partially molten silicates^{S24}, c_P the heat capacity, L is the depth of the magma ocean and k is the standard thermal conductivity.

Using this result, we can compute an effective thermal conductivity k_{eff} in order to simulate the efficient heat loss from the magma ocean:

$$k_{eff} = \left(\frac{q}{0.089} \right)^{3/2} \frac{1}{(T - T_{surf})^2 \rho} \left(\frac{\alpha g c_P}{\eta_{part}} \right)^{-1/2} \quad (3)$$

where η_{part} is the viscosity of the partially molten silicates in the numerical model.

As the viscosity of molten iron is also very small ($\eta_{Fe} = 10^{-2}$ Pa s)^{S38}, the same method is applied to take into account the cooling of the molten iron-sulphide material. For all physical parameters see also Supplementary Table S3.

Supplementary Table S2: Model Overview

Name	t_{start} [Ma]	r_{Fe} [km]	η_{part} [Pa s]
vesta1	0	25	10^{17}
vesta2	0	15	10^{17}
vesta2a	0.5	15	10^{17}
vesta2b	1.0	15	10^{17}
vesta2c	2.0	15	10^{17}
vesta2d	1.5	15	10^{17}
vesta2e	0.5	15	10^{16}
vesta2f	0.5	15	10^{18}
vesta3	0	10	10^{17}

t_{start} is the time after CAI formation at which the non-accreting planetesimal formed instantaneously. r_{Fe} is the radius of the iron diapirs randomly distributed throughout the interior of the planetesimal. η_{part} is the viscosity of partially molten silicates for melt fractions below the critical melt fraction ζ_{crit} .

Supplementary Table S3: Physical Parameters

Parameter	Symbol	Value	Units
Radius of Vesta-sized planetesimal	R_P	2.65×10^5	m
Iron-sulphide diapir radii	r_{Fe}	$(1.0-2.5) \times 10^4$	m
Density of uncompressed iron-sulphide eutectic	ρ_{Fe}	7540	kg m^{-3}
Density of uncompressed solid silicates	ρ_{Si-sol}	3500	kg m^{-3}
Density of uncompressed silicate melt	ρ_{Si-liq}	2900	kg m^{-3}
Initial temperature after accretion	T_{init}	310	K
Cohesion	χ	10^8	Pa
Sine of friction angle	$\sin(i)$	0.3	
Activation energy	E_a	532	kJ mol^{-1}
Activation volume	V_a	8.0×10^{-6}	$\text{m}^3 \text{mol}^{-1}$
Dislocation creep onset stress	σ_0	3.0×10^7	Pa
Power law exponent	n	3.5	
Latent heat of silicate melting	L_{Si}	400	kJ kg^{-1}
Latent heat of iron-sulphide melting	L_{Fe}	240	kJ kg^{-1}
Silicate melt fraction at rheological transition	ξ_{crit}	0.4	
Heat capacity	c_P	1000	$\text{J kg}^{-1} \text{K}^{-1}$
Thermal expansivity of solid silicates	α_{Si-sol}	3.0×10^{-5}	K^{-1}
Thermal expansivity of molten silicates	α_{Si-liq}	6.0×10^{-5}	K^{-1}
Thermal expansivity of iron material	α_{Fe}	1.0×10^{-5}	K^{-1}
Thermal conductivity of solid materials	k	3.0	$\text{W m}^{-1} \text{K}^{-1}$
Effective thermal conductivity of molten materials	k_{eff}	$\leq 1.0 \times 10^6$	$\text{W m}^{-1} \text{K}^{-1}$

S4 Supplementary References

- [S1] Boudier, F. Olivine xenocrysts in picritic magmas. *Contrib. Mineral Petrol.* **109**, 114-123 (1991)
- [S2] Ismail, W.B. & Mainprice, D. An olivine fabric database: an overview of upper mantle fabrics and seismic anisotropy. *Tectonophysics* **296**, 145-157 (1998).
- [S3] Tommasi A., Mainprice D., Canova, G. & Chasatel, Y. Viscoplastic self-consistent and equilibrium-based modeling of olivine lattice preferred orientations: Implications for the upper mantle seismic anisotropy. *J. Geophys. Res.* **105**, 7893-7908 (2000).
- [S4] Frese, K., Trommsdorff, V., Kunze, K. Olivine [100] normal to foliation: lattice preferred orientation in prograde garnet peridotite formed at high H₂O activity, Cima di Cagnone (Central Alps). *Contrib. Mineral Petrol.* **145**, 75-86 (2003)
- [S5] Jung, H., Katayama, I., Jiang, Z., Hiraga, T., Karato, S. Effect of water and stress on the lattice-preferred orientation of olivine. *Tectonophysics* **421**, 1-22 (2006)
- [S6] Holtzman, B.K. et al. Melt Segregation and Strain Partitioning: Implications for Seismic Anisotropy and Mantle Flow. *Science* **301**, 1227-1230 (2003).
- [S7] Schiller, M., et. al.. Rapid Timescales for Magma Ocean Crystallization on the Howardite-Eucrite-Diogenite Parent Body. *Astrophys. J. Lett.* **740**, L22 (2011).
- [S8] Day, J. M. D., Walker, R. J., Qin, L. & Rumble, D. Late accretion as a natural consequence of planetary growth. *Nature Geoscience* **5**, 614-617 (2012)
- [S9] Ghosh, A. & McSween, H. Y. A Thermal Model for the Differentiation of Asteroid 4 Vesta, Based on Radiogenic Heating. *Icarus* **134**, 187-206 (1998).
- [S10] Jutzi, M. & Asphaug, E. Mega-Ejecta on Asteroid Vesta. *Geophys. Res. Lett.* **38**, L01102 (2011).
- [S11] Gerya, T. V. & Yuen, D. A. Robust characteristics method for modelling multiphase visco-elasto-plastic thermo-mechanical problems. *Phys. Earth Planet. Int.* **163**, 83-105 (2007).
- [S12] Thomas, P. C. et al. Vesta: Spin pole, size and shape for the HST images. *Icarus* **128**, 88-94 (1997b).
- [S13] Johansen, A. et al. Rapid planetesimal formation in turbulent circumstellar disks. *Nature* **448**, 1022-1025 (2007).
- [S14] Schmeling, H., et al. A benchmark comparison of spontaneous subduction models - Towards a free surface. *Phys. Earth Planet. Int.* **171**, 198-223 (2008).
- [S15] Lin, J.-R., Gerya, T. V., Tackley, P. J., Yuen, D. A. & Golabek, G. J. Numerical modeling of protocore destabilization during planetary accretion: Methodology and results. *Icarus* **204**, 732-748 (2009).
- [S16] Golabek, G. J. et al. Origin of the Martian dichotomy and Tharsis from a giant impact causing massive magmatism. *Icarus* **215**, 346-357 (2011).

- [S17] Crameri, F. *et al.* A comparison of numerical surface topography calculations in geodynamic modelling: an evaluation of the 'sticky air' method. *Geophys. J. Int.* **189**, 38-54 (2012).
- [S18] Touboul, M., Kleine, T. & Bourdon, B. Hf-W systematics of cumulate eucrites and the chronology of the eucrite parent body. *Lunar Planet. Sci.* **XXXIX**, 2336 (2008).
- [S19] Kleine, T. *et al.* Hf-W chronology of the accretion and early evolution of asteroids and terrestrial planets. *Geochim. Cosmochim. Acta* **73**, 5150-5188 (2009).
- [S20] Ranalli, G., *Rheology of the Earth*. Second ed., Chapman & Hall, London, UK, 436pp. (1995).
- [S21] Schubert, G., Spohn, T & Reynolds, R. T. Thermal histories, compositions and internal structures of the moons of the solar system. In: J. A. Burns and M. S. Matthews (Eds.), *Satellites*, Arizona University Press, 224-292 (1986).
- [S22] Chudinovskikh, L., & R. Boehler, Eutectic melting in the system Fe-S to 44 GPa. *Earth Planet. Sci. Lett.* **257**, 97-103 (2007).
- [S23] Herzberg, C., Ratteron, P. & Zhang, J. New experimental observations on the anhydrous solidus for peridotite KLB-1. *Geochem. Geophys. Geosyst.* **1**, 2000GC000089 (2000).
- [S24] Wade, J. & Wood, B. J. Core formation and the oxidation state of the Earth. *Earth Planet. Sci. Lett.* **236**, 78-95 (2005).
- [S25] Burg, J.-P. & Gerya, T. V. The role of viscous heating in Barrovian metamorphism of collisional orogens: thermomechanical models and application to the Lepontine Dome in the Central Alps. *J. Metamorp. Geol.* **23**, 75-95 (2005).
- [S26] Barr, A. C. & Canup, R. M. Constraints on gas giant satellite formation from the interior states of partially differentiated satellites. *Icarus* **198**, 163-177 (2008).
- [S27] Costa, A., Caricchi, L. & Bagdassarov, N. A model for the rheology of particle-bearing suspensions and partially molten rocks. *Geochim. Geophys. Geosyst.* **10**, Q03010 (2009).
- [S28] Solomatov, V. S. Magma Oceans and Primordial Mantle Differentiation. *Treatise on Geophysics.* **9**, 91-119, (2007).
- [S29] Reese, C. C., Orth, C. P. & Solomatov, V. S. Impact origin for the martian crustal dichotomy: Half-emptied or half-filled? *J. Geophys. Res.* **115**, E05004 (2010).
- [S30] Rubie, D., Melosh, H. J., Reid, J. E., Liebske, C. & Richter, K. Mechanisms of metal-silicate equilibration in the terrestrial magma ocean. *Earth Planet. Sci. Lett.* **205**, 239-255 (2003).
- [S31] Liebske, C. *et al.* Viscosity of peridotite liquid up to 13 GPa: Implications for magma ocean viscosities. *Earth Planet. Sci. Lett.* **240**, 589-604 (2005).
- [S32] Kushiro, I. Viscosity of partial melts in the upper mantle. *J. Geophys. Res.* **91**, 9343-9350 (1986).
- [S33] Zahnle, K. J., Kasting, J. F. & Pollack, J. B. Evolution of a steam atmosphere during Earth's accretion. *Icarus* **74**, 62-97 (1988).

Solid-state plastic deformation in the dynamic interior of a differentiated asteroid

B. J. Tkalcec^{1*}, G. J. Golabek^{2,3}, F. E. Brenker¹

- [S34] Tackley, P. J., Schubert, G., Glatmaier, G. A., Schenk, P. & J. T. Ratcliff. Three-Dimensional Simulations of Mantle Convection in Io. *Icarus* **149**, 79-93 (2001).
- [S35] Hevey, P. J. & Sanders, I. S. A model for planetesimal meltdown by ²⁶Al and its implications for meteorite parent bodies. *Meteorit. Planet. Sci.* **41**, 95-106 (2006).
- [S36] Kraichnan, R. H. Turbulent thermal convection at arbitrary Prandtl number. *Phys. Fluids* **5**, 1374-1389 (1962).
- [S37] Siggia, E. D. High Rayleigh number convection. *Annu. Rev. Fluid Mech.* **26**, 137-168 (1994).
- [S38] Rubie, D. C., Nimmo, F. & Melosh, H. J. Formation of the Earth's core. *Treatise on Geophysics* **9**, 51-90 (2007).